hydrology

MDPI

Article

Beyond Vertical Accuracy: Benchmarking Global DEMs for Hydrologic Connectivity and Flood Sensitivity in Flat Coastal Plains

Jose Miguel Fragozo Arevalo, Jairo R. Escobar Villanueva * and Jhonny I. Pérez-Montiel

Grupo de Investigación GISA, Facultad de Ingeniería, Universidad de La Guajira, km 3 + 354 Vía a Maicao, Riohacha 440007, Colombia; jmfragozo@uniguajira.edu.co (J.M.F.A.); jpemon@uniguajira.edu.co (J.I.P.-M.)
* Correspondence: jrescobar@uniguajira.edu.co

Abstract

We assessed the vertical accuracy of six global digital elevation models—FABDEM (SRTM-enhanced), SRTM, ASTER GDEM, ALOS AW3D30, DeltaDTM and GEDTM—against a local photogrammetry-derived DEM as a benchmark in a flat coastal plain of the Colombian Caribbean. Using GNSS-RTK ground points and a high-accuracy reference DEM, we computed BIAS, RMSE, and MAE. Errors were analyzed by land cover class and along transverse profiles relative to the reference DEM. We also evaluated hydrologic suitability by comparing flow accumulation and drainage patterns derived from each model, treating the photogrammetry-derived model as the control and the global DEMs as treatments to gauge their ability to represent hydraulic/hydrologic behavior. DeltaDTM, GEDTM and FABDEM showed the best overall performance, with the lowest vertical error (particularly in non-urban areas with sparse vegetation) and the highest drainage agreement, along with their flood extent sensitivity to a 0.5 m water level rise, all of which were comparable to the benchmark. These results provide practical guidance for selecting and preprocessing topographic models for risk management and territorial planning in flat regions.

Keywords: DEM; GNSS-RTK; vertical accuracy; land cover; floodplains; hydrologic connectivity

1. Introduction

Floodplains are defined as the flat area (slope less than 3%) surrounding the active channel of a river, which floods during river flood events every one or two years [1]. Within these floodplains are deltas, alluvial plains, and valleys [2,3]. These are areas conducive to economic development, agriculture, and community settlement [4], with those with a humid and rainy climate being the most fertile and affected by flooding [5]. Floodplains are topologically and dynamically complex areas [6]. In addition to the natural complexity of these areas, there is also anthropogenic pressure on them, as their location makes them suitable for economic development, agriculture, and community settlement [4]. In recent decades, population growth in floodplains [7], along with more extreme and intense rainfall events caused by phenomena such as El Niño/La Niña [8], has increased the risk of flooding in many of these places around the world [7]. Given this scenario, it is necessary to implement risk reduction strategies, which require high-quality inputs and the use of tools that generate useful information for decision-making [8].

"DEM" (digital elevation model) is the general term for a digital representation of the elevations (or height) of a topographic surface in the form of a georeferenced grid

Academic Editor: Aristoteles Tegos

Received: 15 December 2025
Revised: 5 February 2026
Accepted: 19 February 2026
Published: 22 February 2026

based on points or areas, covering the earth or other solid celestial bodies. Currently, the most common DEMs use rectangular grids ("arrays") and raster image file storage formats. Alternative structures for digital topography, such as triangulated irregular networks (TINs), contours, and point clouds, are not DEMs as defined here because they are not grids [9]. DEMs can be classified into two basic types: digital surface models (DSMs), which correspond to the heights of the terrain and everything on it (buildings, houses, structures, vegetation, etc.), and the corrected digital terrain model (DTM), which corresponds to the heights of the terrain without structures, also known as a bare ground model [10]. The most commonly used methodologies for generating digital models of DEM elevation data sources are: (i) contour maps obtained through terrestrial surveys; (ii) light detection and ranging (LiDAR) using aerial laser scanning; and (iii) spatial data, such as those from Cartosat-1, ASTER (Advanced Spaceborne Thermal Emission and Reflection Radiometer), and SRTM [11]. Each of these data sources for DEM generation has its advantages and disadvantages. DEMs from satellite sources have wide coverage and are easy to acquire, but they lack detail and can be subject to high levels of noise due to canopy vegetation, which masks the bare ground below. DEMs obtained from airborne equipment have greater accuracy but low coverage and high acquisition costs, while LiDAR can achieve a much more refined level of detail, but its availability is very limited, and acquisition is more complex and costly [12].

DEMs are widely used in geosciences [13] and are one of the main sources of raster (matrix) elevation data for multiple applications in the field of land use planning and risk management [14]. An altimetrically reliable DEM is one of the most important inputs for land use planning and flood risk management applications [10]. This problem becomes more critical in flat areas where low-precision models cannot represent the terrain configuration in sufficient detail [15]. Applications such as defining flood zones, delimiting waterways, defining restoration areas, and estimating flood threats require a high-quality DEM, with a spatial resolution of 10 m or better, with vertical accuracy in the range of tens of centimeters. These DEMs are essential for applications requiring high precision, such as urban planning, flood risk management, and detailed environmental monitoring [16]. These applications use modeling tools for which this input is of great importance, since the reliability of predicting the extent and depth of flooding depends on its vertical accuracy [17,18]. However, in many parts of the world, the availability of high-resolution DEMs is limited [19].

Risk management and land use planning applications rely mainly on low- and medium-resolution global DEMs [20,21], such as SRTM (Shuttle Radar Topography Mission) [22,23], Earth Resources Observation And Science (EROS), ASTER Global DEM [24,25], ALOS PALSAR [26], TANDEM-X DEM [27], COPERNICUS DEM [28] and FABDEM [29,30]. These DEMs have vertical errors that can vary between 1.2 and 10 m [30,31]. This makes it imperative to analyze their accuracy in order to determine the most suitable one for land use planning and risk management applications [21].

However, relying solely on vertical error metrics provides an incomplete picture of a DEM's suitability for hydrodynamic applications [32]. In low-relief terrain, the surface roughness inherent to standard DSMs can act as an artificial flow barrier; therefore, assessments must go beyond vertical accuracy to include hydrologic connectivity and flood sensitivity metrics that capture actual hydraulic behavior [33]. However, despite the growing availability of bare-earth products, their hydrologic gains over legacy DSMs in flat tropical settings remain sparsely validated. In parallel, several next-generation ML-corrected terrain datasets (e.g., DeltaDTM, DiluviumDEM, GEDTM30, and FathomDEM) have reported improved coastal or global bare-earth performance, although some have licensing constraints or region-specific scopes.

Consequently, this study benchmarks the hydrologic connectivity and flood sensitivity of four global DEMs (FABDEM as a freely accessible global DTM and SRTM, ASTER, and ALOS as widely used legacy DSMs) in the flat coastal plains of the Guajira Peninsula (Colombian Caribbean). By validating these models against field surveys and a high-resolution photogrammetric benchmark, we quantify the impact of artifact removal on both vertical accuracy and flood propagation, assessing the suitability of these DEMs for local risk management in data-scarce environments.

2. Materials and Methods

2.1. Study Area

The study area corresponds to the Ranchería River delta in the city of Riohacha, La Guajira, Colombia. The Ranchería River delta is located northeast of the city. Figure 1 shows the general location and the course of the main channel of the Ranchería River (1), which branches off near the coastline, giving rise to two arms that form the delta, El Riíto (2) and Santa Rita (3), the latter of which branches off again to give rise to the Calancala branch (4) [34].

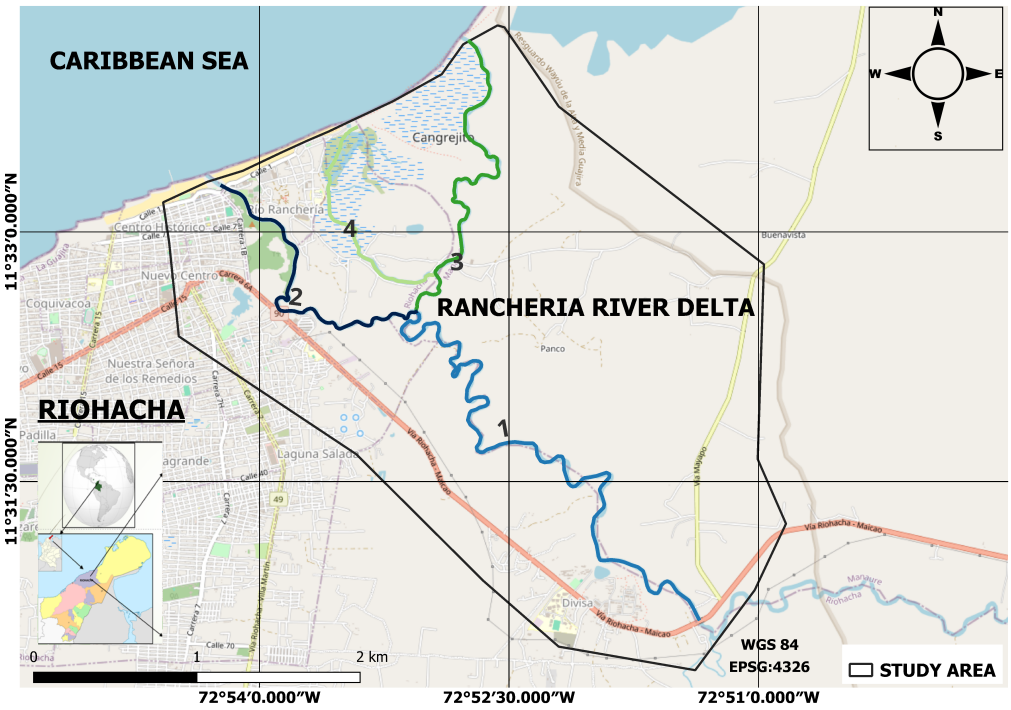

Figure 1. The location of the Ranchería River delta with respect to the urban area of Riohacha and its discharge to the Caribbean Sea.

2.2. Data Used

2.2.1. Digital Elevation Models (DEMs)

- Reference DEM (DEM-FA). This model was generated using photogrammetry and DTM correction, with images taken from a manned aircraft. A survey was conducted by the Colombia Adaptation Fund for the municipalities of Riohacha, Maicao, and Manaure in La Guajira, Colombia, in 2017. This DEM has a spatial resolution of 1 m and was resampled to 30 m to make it comparable to other global DEMs [35].
- SRTM (Shuttle Radar Topography Mission). This mission was carried out over 11 days in February 2000, collecting data from the C-band synthetic aperture radar (SAR) C on land areas between 60° N and 56° S, representing about 80% of the total land mass as a

digital surface model (DSM) in which vegetation and buildings remain [23]. Version 3 of the SRTM DEM with 30-meter spatial resolution, published in 2015, was used [22].

- ALOS (ALOS WORLD 3D DEM). Between 2006 and 2011, the Panchromatic Remote-sensing Instrument for Stereo Mapping (PRISM) sensor aboard the ALOS satellite (Japan Aerospace Exploration Agency) captured stereoscopic images with a resolution of 2.5 m [26,36]. These images were used to produce a very-high-resolution (0.15 arcseconds) commercial DSM, ALOS World 3D (AW3D), which was subsequently resampled to obtain the freely accessible ALOS World 3D 30 m (AW3D30) DEM, with a resolution of 30 m [26,36]. The latest available version 3.2 was used [37].
- ASTER GDEM. The Global Digital Elevation Model (GDEM) Version 3 (ASTGTM) from the Advanced Spaceborne Thermal Emission and Reflection Radiometer Terra's ASTER provides a global digital elevation model (DEM) of the earth's land areas with a spatial resolution of 30 m [24,38].
- FABDEM (Forest And Buildings removed DEM). This is a global digital terrain model derived from the Copernicus DEM. It has a spatial resolution of 30 m and covers latitudes in the range of ±60°. Its development was based on machine learning techniques trained with LiDAR data and land cover layers, which significantly improves accuracy in forested and urban areas compared to other similar models [29].
- DeltaDTM is a global coastal digital terrain model (DTM) available in the public domain, with a horizontal spatial resolution of 1 arcsecond (~30 m) and a vertical mean absolute error (MAE) of 0.45 m overall. DeltaDTM is a global coastal DTM based on a fusion of CopernicusDEM, ICESat-2, and GEDI elevation data. The vertical biases of surface data (e.g., canopy, buildings) present in CopernicusDEM were removed by using ICESat-2 and GEDI terrain elevation measurements [39].
- Global Ensemble Digital Terrain Model 30 m (GEDTM30) is a 1-arcsecond (30 m) global digital terrain model (DTM) generated using machine learning-based data fusion. It was trained using a global-to-local Random Forest model with ICESat-2 and GEDI data, incorporating almost 30 billion high-quality points [40].

Figure 2 shows the cropping of the reference DEM to the study area, and Figure 3 shows the cropping of the used global DEMs to the study area.

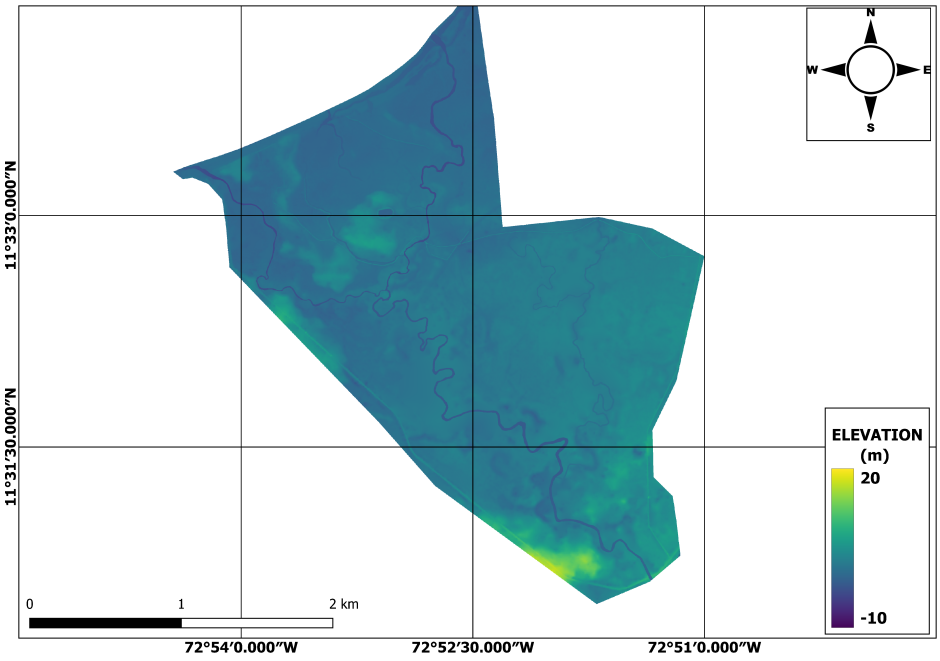

Figure 2. Reference DEM.

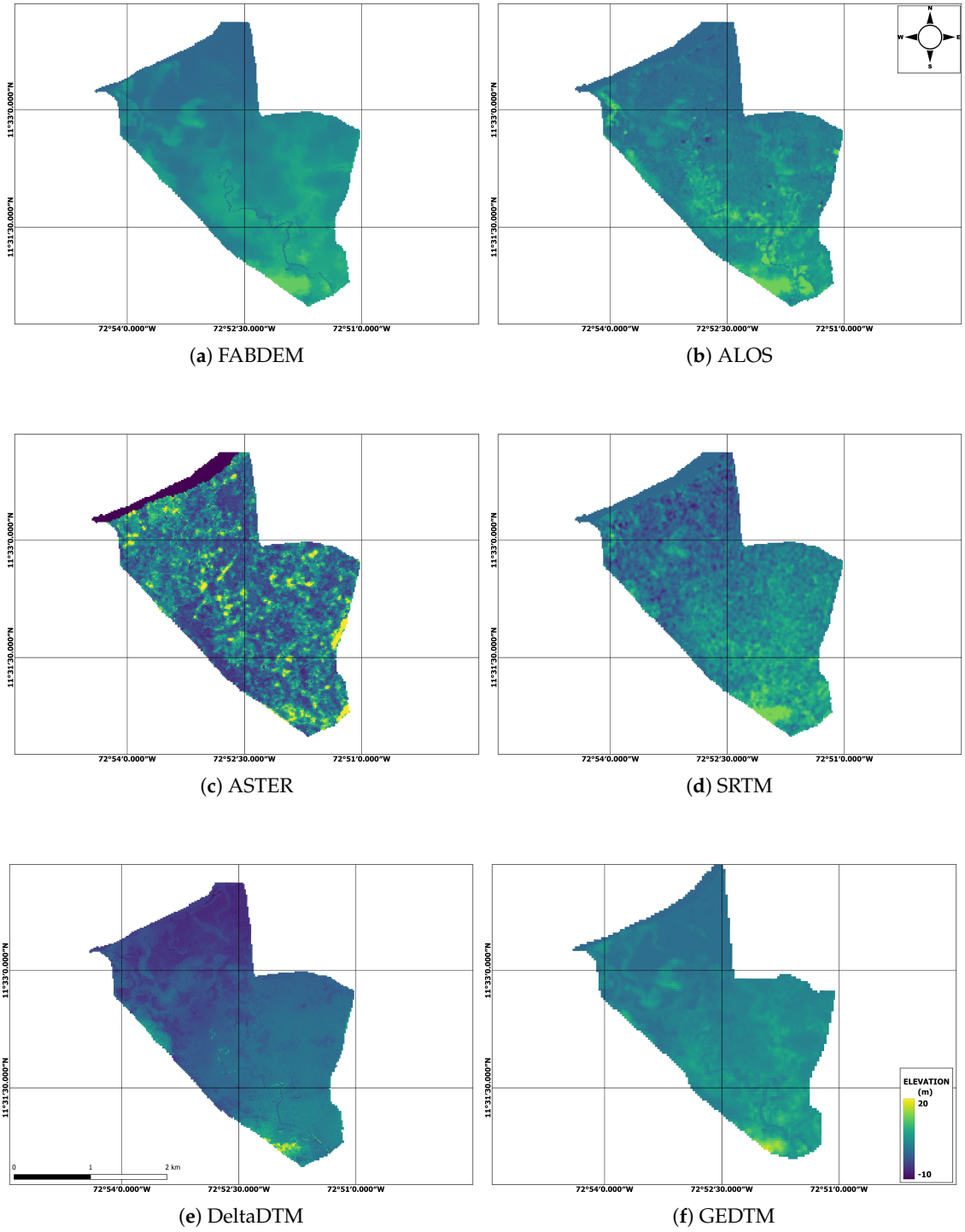

(**a**) FABDEM (**b**) ALOS

(**c**) ASTER (**d**) SRTM

(**e**) DeltaDTM (**f**) GEDTM

Figure 3. Used global DEMs.

2.2.2. Land Cover Information

The European Space Agency (ESA) coverage map, ESA WorldCover 2021 v200 [41], was used as a basis to generate a land cover map of the study area; this can be seen in Figure 4.

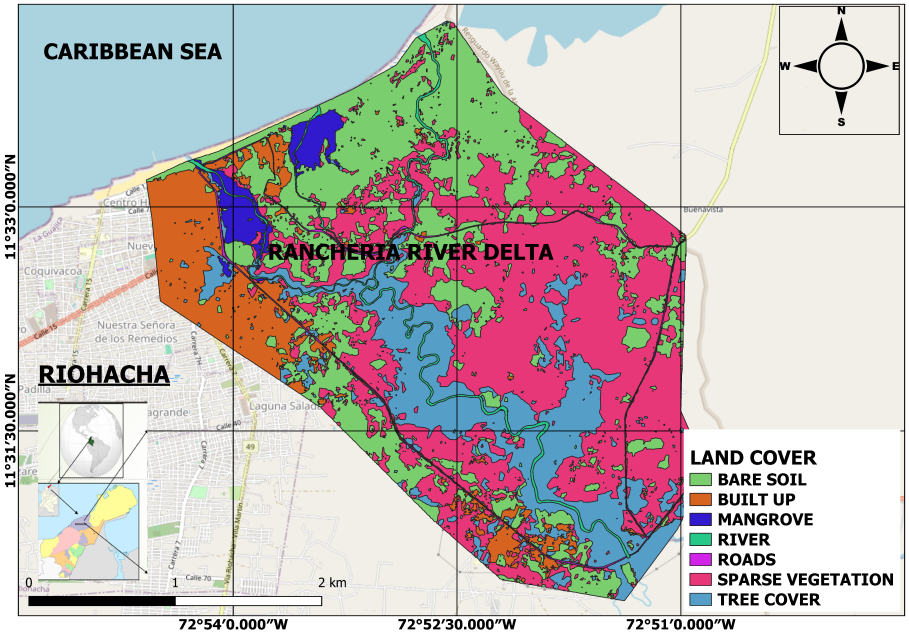

Figure 4. Land cover map of study area.

2.2.3. Topographic Information

Field topographic information was obtained from two campaigns carried out by the research team in the study area, one in September 2022 and the other in March 2023. Topographic points were surveyed with GNSS-RTK in dynamic mode, using TOPCON Hyper V equipment, which has a horizontal accuracy of 0.005 m and a vertical accuracy of 0.01 m [42]. These GNSS-RTK checkpoints provide an independent, high-precision reference for evaluating meter-scale DEM errors in low-relief settings, as we study deltaic floodplains. A total of 680 ground control points were used to evaluate the elevation models. Checkpoints may be accessibility-biased (e.g., closer to roads/levees), potentially undersampling densely vegetated or flooded zones; this is a common constraint in data-scarce floodplains and is considered when interpreting class-based results. Figure 5 shows the location of the points.

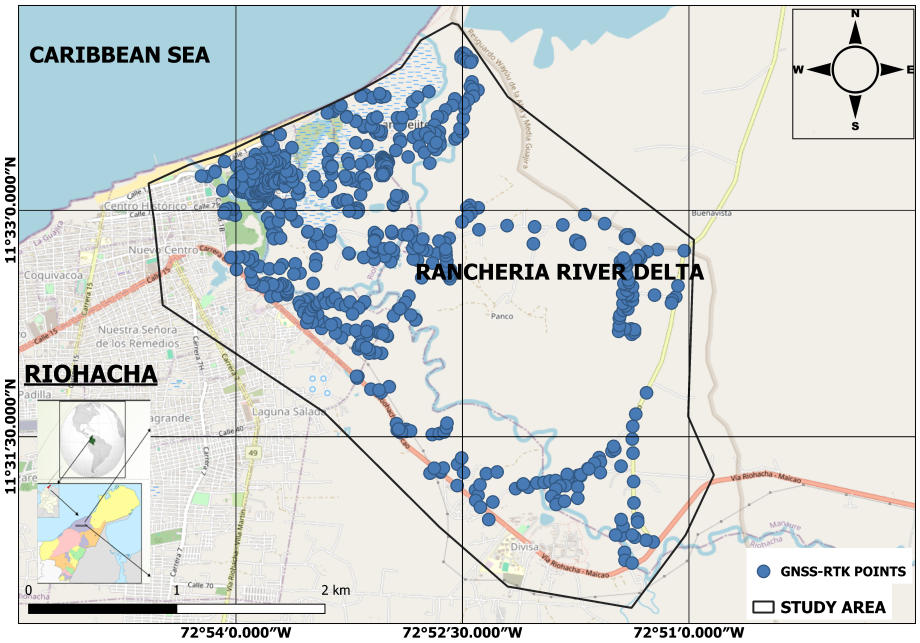

Figure 5. The topographic points surveyed in the study area.

2.3. Vertical Accuracy Assessment of DEMs

2.3.1. Preprocessing

Before evaluating the DEMs with the points, the process of outlier removal was carried out to eliminate random errors in the DEM, which can alter error metrics. This correction is made by applying a conservative 3-sigma despiking criterion to remove extreme elevation artifacts. This step was applied consistently to all DEMs to ensure comparability. This criterion indicates that all values in a data distribution must be located between the limits, average −3 standard deviations to average +3 standard deviations, and any value outside these limits is considered an outlier [43–46]. This process was performed using an algorithm that scans the DEM pixel by pixel, comparing the value with the 3-sigma calculated for that DEM. When it finds a pixel with a higher value, that value is replaced by the 3-sigma value.

2.3.2. Error Calculation and Error Metrics

For the vertical accuracy assessment of DEMs, first, the elevation of the DEM is extracted at each point; then the error is calculated with Equation (1).

$$\Delta Z = Z_{ref} - Z_{DEM} \tag{1}$$

The following commonly used metrics for the vertical accuracy of DEMs were used: the MAE (mean absolute error) [29,47] (Equation (2)); $RMSE$ (Root Mean Square Error) [10,48–50] (Equation (3)); $BIAS$ (Equation (4)), which measures the average tendency of the model data to overestimate or underestimate the true value (field data) [49]; and STD (standard deviation) (Equation (5)) [21].

$$MAE = \frac{1}{n}\sum_{i=1}^{n}|\Delta Z_i| \tag{2}$$

$$RMSE = \sqrt{\frac{1}{n}\sum_{i=1}^{n}\Delta Z_i^2} \tag{3}$$

$$BIAS = \frac{\sum_{i=1}^{n}\Delta Z_i}{\sum_{i=1}^{n} Z_{ref}} \tag{4}$$

$$STD = \sqrt{\frac{1}{n-1}\sum_{i=1}^{n}(\Delta Z_i - ME)} \tag{5}$$

where Z_{ref}: elevation of the surveyed point; Z_{DEM}: elevation of the point extracted from the DEM; n: number of points evaluated; ME: mean error.

Errors and metrics were calculated for the whole area without filtering or classification and for each land cover class. Classes corresponding to bodies of water (rivers) were excluded from the analysis.

2.4. Assessing the Hydrological Connectivity DEM Performance

2.4.1. Comparison of DEM Drainage Networks Using Double-Buffer Method (DBM) and P–R–F1 Metrics

Drainage networks derived from global DEMs were compared against a high-resolution benchmark reference using the double-buffer method (DBM) [51]. The double-buffer method (DBM) aims to compare drainage networks derived from different DEMs: for a buffer distance d, buffers are generated around both the benchmark and the candidate, and positional agreement is quantified by the length of their intersection. Let S_{ref} be the DEM benchmark stream network and S_{cand} the DEM candidate. For a buffer width d, we

construct buffers B_{ref} d around S_{ref} and B_{cand} d around S_{cand}. The following length-based metrics are then computed: precision (6), recall (7) and F1 score (8).

$$Precision(P) = \frac{L(S_{cand} \bigcap B_{ref}(d))}{L(S_{cand})} \quad (6)$$

$$Recall(R) = \frac{L(S_{ref} \bigcap B_{cand}(d))}{L(S_{ref})} \quad (7)$$

$$F_1 score = \frac{2PR}{P+R} \quad (8)$$

The automation of the GIS (QGIS Desktop 3.40.12) [52] workflow consisted of the following steps: Import DEMs → Streamline generation → Fix/Dissolve → Buffers → Clip (to obtain $S_{cand} \cap B_{ref}$ and $S_{ref} \cap B_{cand}$) → Length calculation → Join → P/R/F1 → Export statics (*.csv). We evaluated multiple d values (15, 21.213, 30 m) to reflect positional tolerance at 30 m DEM resolution.

2.4.2. Benchmark Agreement and Water Level Sensitivity Analysis via Static Flood Assessment

Complementary to geometric drainage spatial analysis, a static inundation was conducted following the simple bathtub model approach [53]. This method delineates potentially inundated areas by projecting a fixed water level onto the terrain surface in flood-prone areas like coastal deltas using only DEM data as input in a GIS raster calculator. In this study, bathtub analysis was applied over the same study area DEM mask used to crop all products to the Ranchería delta domain (Figure 1), ensuring a common spatial extent across models. We compared the flood extents generated by each candidate DEM against the benchmark, assessing hydrological connectivity and the sensitivity of each model to vertical water level increments in hypothetical scenarios: base at 0 m and expansion at 0.5 m above sea level flood inundation.

Bathtub classification was applied over the clipped deltaic lowland study extent (flood-prone coastal plain) shown in Figure 1, using constant water levels of 0.0 and 0.5 m above sea level as hypothetical scenarios. We used this static inundation approach as a controlled, comparative sensitivity framework rather than a predictive hydrodynamic model. It was applied to isolate and compare the relative flood extent response of each DEM under identical water level scenarios [54].

2.4.3. Surface Roughness and Roughness Inflation Index (RII)

To provide a compact diagnostic of micro-topographic variability relevant to floodplain connectivity, we computed surface roughness for each DEM on the harmonized 30 m grid using a 3 × 3 moving window as the local elevation range (max–min of the central cell and its eight neighbors), as commonly implemented in gdaldem/QGIS and related terrain ruggedness formulations [55]. Roughness values were summarized within the whole study area using the median (robust to spikes), and we defined the Roughness Inflation Index (RII) for each DEM as follows:

$$RII = \frac{MedianRoughnessCandidateDEM}{MedianRoughnessBenchmarkDEM} \quad (9)$$

We interpret $RII > 1$ as inflated roughness relative to the benchmark (potentially indicating spurious micro-relief that may disrupt connectivity), consistent with recent recommendations to benchmark DEMs using derived land surface parameters in addition to elevation error statistics.

3. Results

3.1. General Vertical Error Assessment

Vertical errors in the DEMs were evaluated using error density curves, verifying that the errors approximate a Gaussian distribution and that the metrics chosen for the analysis are appropriate. Figure 6 shows the error density curves for each of the DEMs and the overall error metrics, including the DEM-FA as the benchmark.

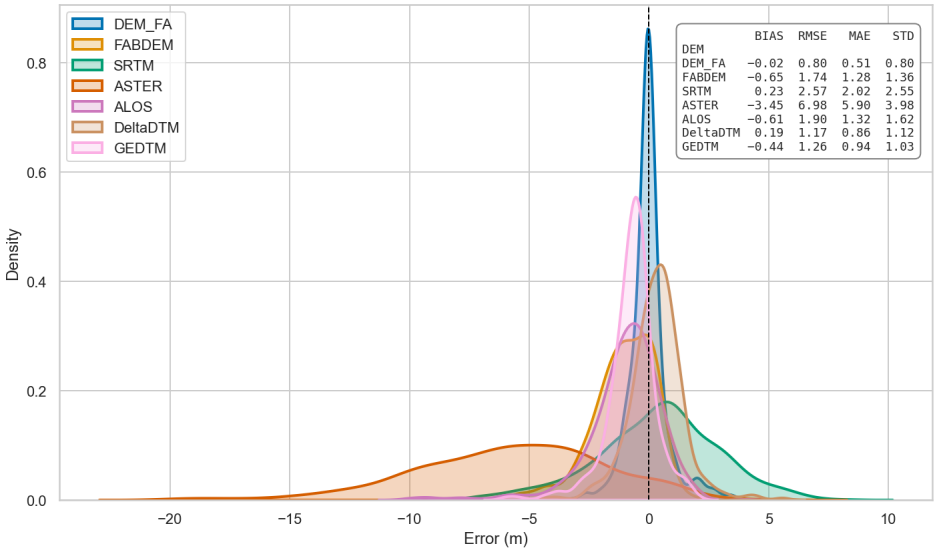

Figure 6. Vertical error probability density curves evaluated against 680 GNSS-RTK checkpoints. The inset displays overall accuracy statistics (*MAE*, *RMSE*, *BIAS*, *STD* in meters) for the full study area.

The results in Figure 6 show that DeltaDTM has the best overall metrics, followed by GEDTM, and in third place is FABDEM, with ASTER having the worst results. The error density curves show that DeltaDTM, GEDTM, and FABDEM have a similar distribution to DEM-FA but with different error magnitudes, with DeltaDTM being the most similar, except in terms of *BIAS*, which is positive and exhibits an opposite tendency. To better observe the results of the error metrics in Figure 7, the six DEMs evaluated are compared with DEM- FA.

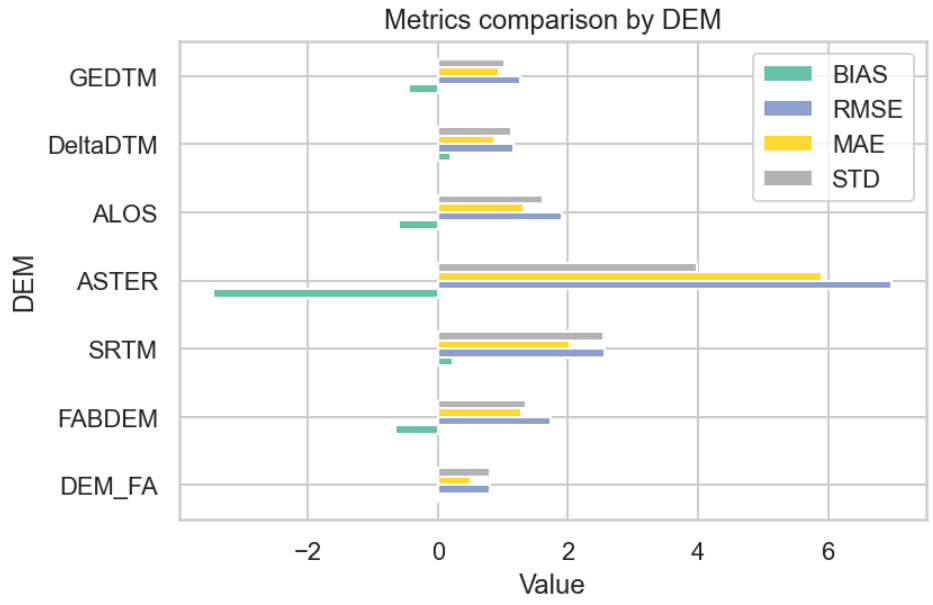

Figure 7. Comparison of error metrics between DEMs.

Comparing the errors with DEM-FA confirms that DeltaDTM has the best overall metrics, followed by GEDTM. However, DeltaDTM does not retain DEM-FA's tendency to overestimate actual heights (negative $BIAS$), while GEDTM conserves the tendency ($BIAS$) of DEM-FA. Although the DeltaDTM and GEDTM metrics are very similar, it is advisable to analyze their errors spatially with respect to DEM-FA and visually analyze which terrain structures can be identified in each one to determine which is the most suitable for use in different applications. To analyze the behavior of DEM errors regarding DEM-FA, cross-sectional profiles were drawn on the terrain to compare the elevation variations between them. The profiles are shown in Figure 8, and Figure 9 shows a comparison of the profiles between global DEMs and DEM-FA.

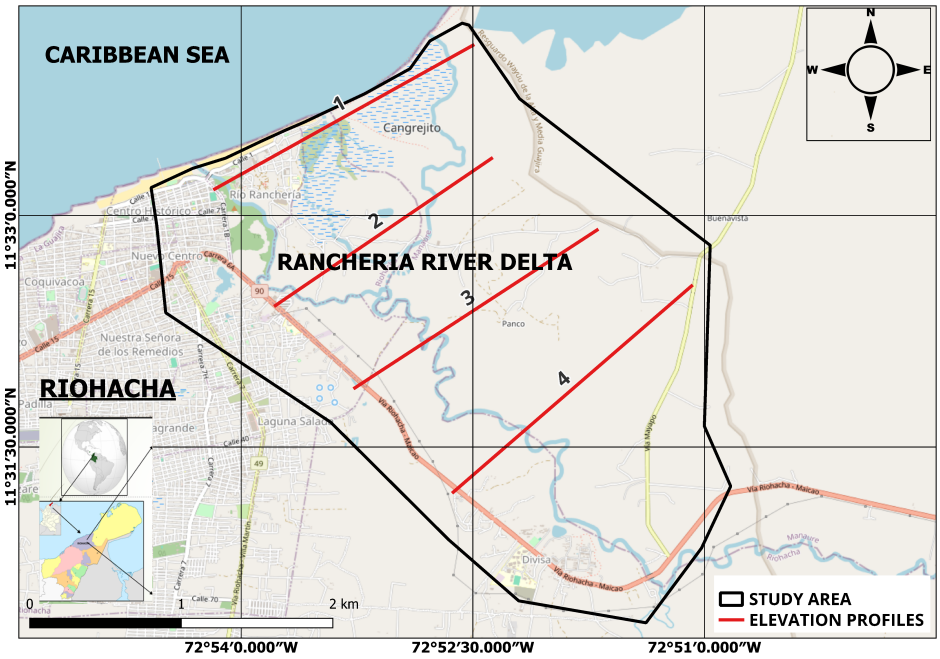

Figure 8. A location map of the four cross-section transects (Profiles 1–4) used for elevation comparison, including GNSS-RTK checkpoints and the Area of Interest (AOI) within the Ranchería River delta.

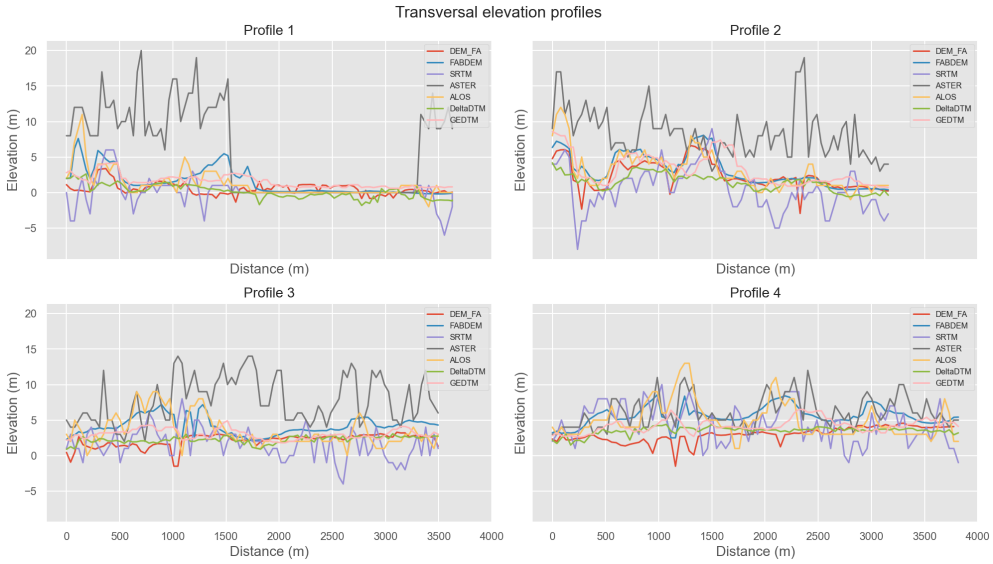

Figure 9. Transversal elevation profiles (corresponding to Figure 8) comparing the benchmark (DEM-FA30) against global DEM candidates. All datasets were sampled on a harmonized 30 m grid.

3.2. Vertical Error Assessment by Land Cover

For the purposes of the evaluation, four coverage classes were selected: bare soil, dense vegetation, sparse vegetation, and buildings. Figure 10 shows a comparison of the error metrics in each of the DEMs evaluated by land cover class. The results show that for DeltaDTM, GEDTM, FABDEM, and ALOS, the categories with the most errors are dense vegetation and sparse vegetation. In SRTM and ASTER, there is a similarity in the contribution of each category to the overall error. The results correspond to the characteristics of the area, where there is considerably less urban cover than vegetation cover.

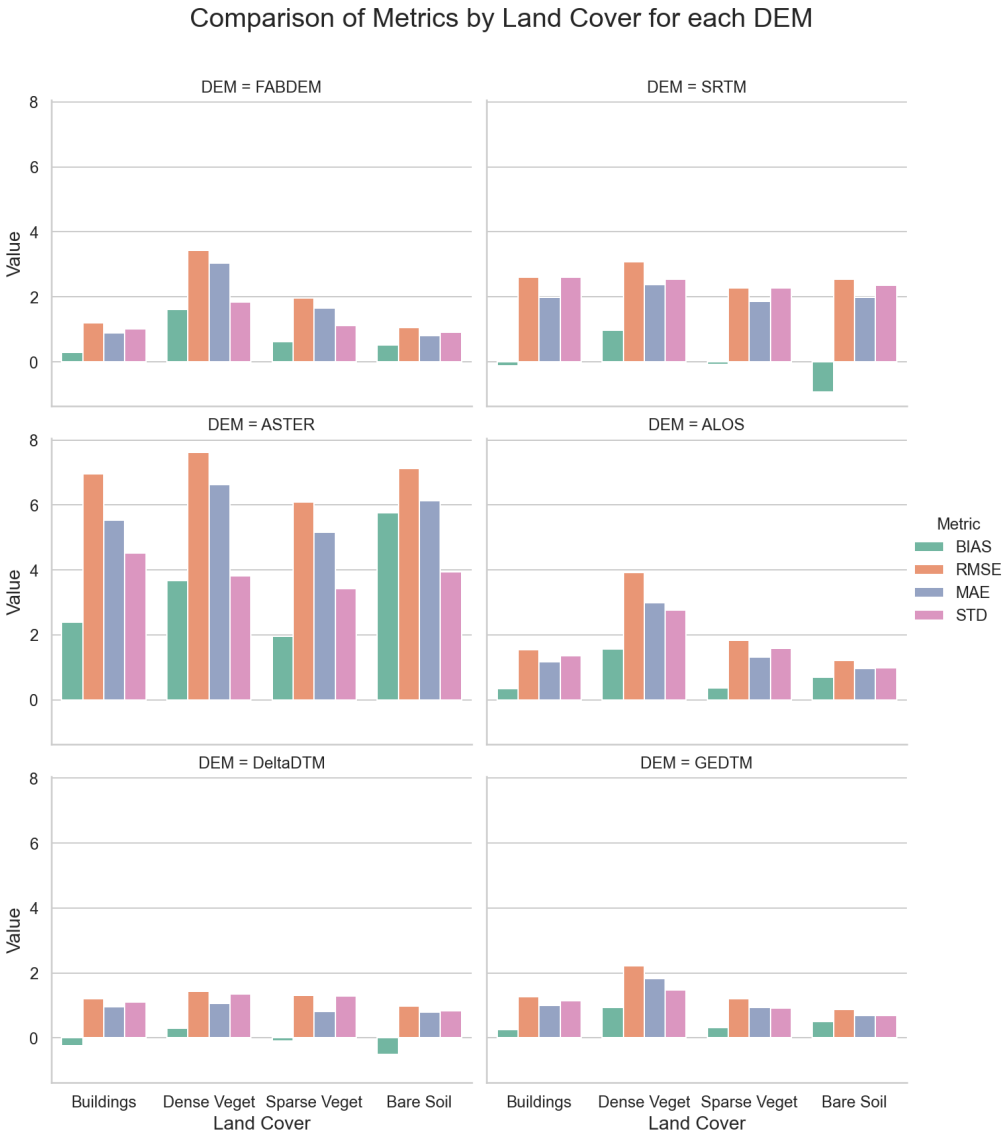

Figure 10. Comparison of error metrics between DEMs by land cover class.

3.3. Global DEM Drainage Comparison Against Local Benchmark Reference DEM

Figure 11 presents a spatial comparison of drainage networks derived from SRTM (orange), FABDEM (red), ASTER (reddish-purple), DeltaDTM (deep purple), GEDTM (dark blue) and ALOS (green) against the benchmark (DEM-FA30, cyan), evaluated using a 30 m positional tolerance via the double-buffer method (DBM; see Section 2.4.1). The results indicate marked performance differences: DeltaDTM, GEDTM, and FABDEM exhibit the highest geometric agreement and continuity (see inset), followed by ALOS, which shows moderate concordance. In contrast, SRTM and ASTER display highly fragmented and

discontinuous traces, indicating a limited ability to reproduce the drainage structure within the study area.

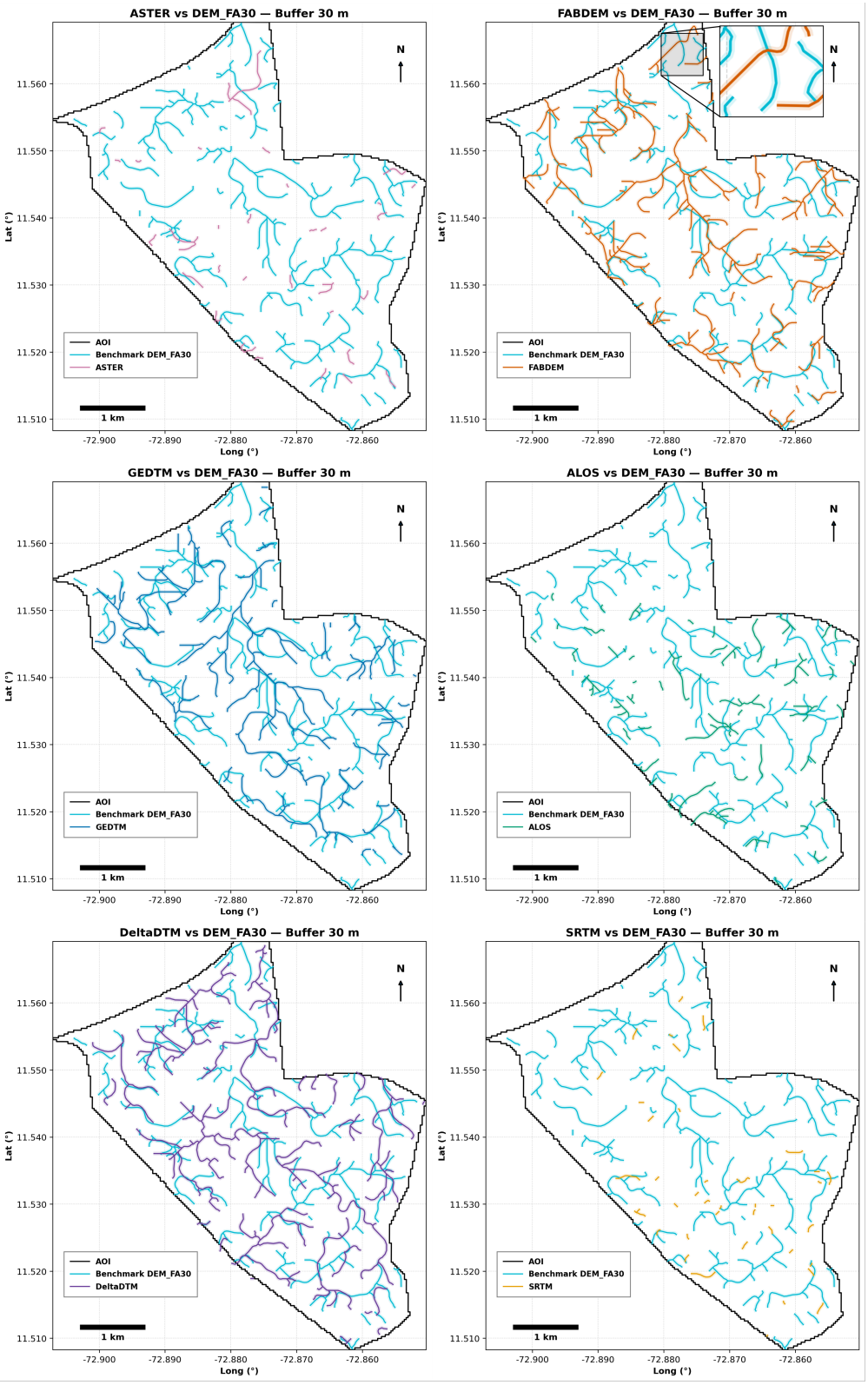

Figure 11. Drainage streamlines derived from each global DEM (colored) compared with the benchmark drainage network derived from DEM-FA30 (cyan), evaluated using the double-buffer method with a 30 m positional tolerance (buffer distance shown in panel titles). The AOI boundary is shown in black; agreement patterns illustrate network continuity and spatial correspondence under the same extraction and tolerance settings.

The metric analysis in Table 1 confirms that FABDEM is the top performer across all buffer widths, with the highest scores at 30 m (F1 = 0.292; P = 0.300; R = 0.285), indicating its superior ability to capture drainage density and preserve network continuity. A second tier is formed by GEDTM and DeltaDTM, which approach the benchmark's agreement at 30 m (F1 = 0.266–0.268; P = 0.260–0.272; R = 0.261–0.276) and show consistent gains from 15 m to 30 m. ALOS exhibits intermediate performance (F1 = 0.124; P = 0.206; R = 0.089 at 30 m): precision is acceptable, but low recall evidences the loss of minor tributaries. In contrast, SRTM and ASTER remain marginal (F1 < 0.05, R $\leq$ 0.028 at 30 m), indicating a limited capacity to delineate fluvial morphology in the study area.

Figure 12 provides a graphical synthesis that demonstrates FABDEM's superior agreement relative to the other models.

Table 1. Comparative performance metrics (precision, recall, F1) for each global DEM at different buffer widths.

DEM	F1 (15 m)	F1 (21m)	F1 (30 m)	P (15 m)	P (21 m)	P (30 m)	R (15 m)	R (21 m)	R (21 m)
FABDEM	0.153	0.216	0.292	0.155	0.22	0.3	0.15	0.213	0.285
ALOS	0.065	0.089	0.124	0.112	0.149	0.206	0.046	0.064	0.089
SRTM	0.021	0.031	0.043	0.1	0.138	0.173	0.012	0.018	0.025
ASTER	0.023	0.034	0.048	0.075	0.111	0.148	0.013	0.02	0.028
GEDTM	0.133	0.191	0.266	0.137	0.195	0.272	0.129	0.187	0.261
DeltaDTM	0.133	0.188	0.268	0.127	0.181	0.26	0.138	0.195	0.276

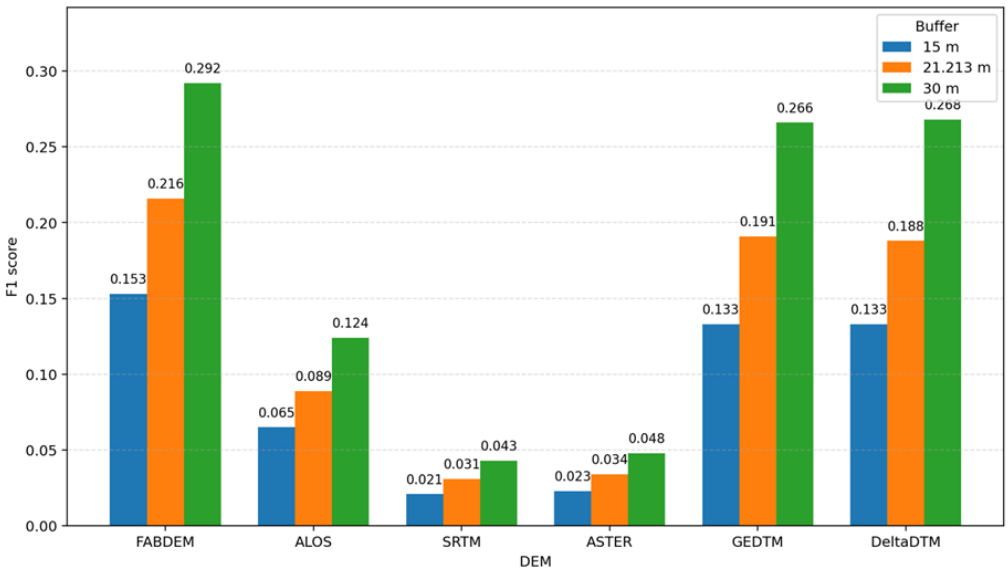

Figure 12. The F1 score of the drainage network agreement between each global DEM and the benchmark (DEM-FA30) computed via the double-buffer method for three positional tolerances (buffer widths: 15 m, 21.213 m, and 30 m). Higher F1 indicates the better geometric agreement and continuity of the extracted drainage network relative to the benchmark.

3.4. Static Flood Assessment Results

The application of the bathtub model at the 0.0 m and 0.5 m elevation thresholds (Figure 13) reveals critical structural contrasts in the representation of low-lying topography. The benchmark (DEM_{FA30}) sets the baseline with a dendritic and connected inundation pattern, displaying a well-defined channel network that expands organically along the northern front and margins as the water level rises.

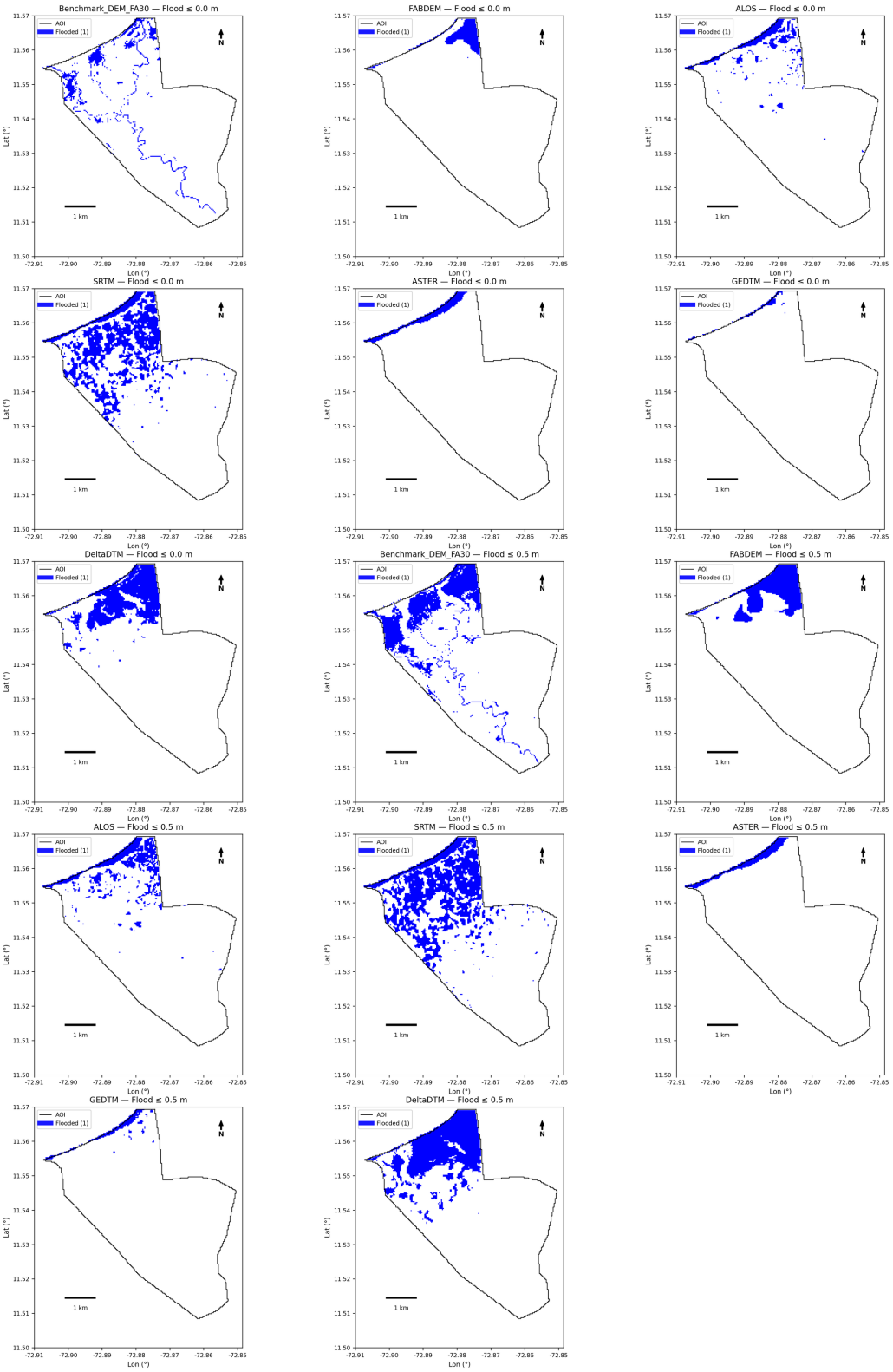

Figure 13. Static inundation (bathtub) flood extents (blue) mapped under two constant water level scenarios, s = 0.0, s = 0.0, s = 0.0 m (baseline) and s = 0.5, s = 0.5, s = 0.5 m (increment), applied over the same clipped deltaic lowland analysis extent for all datasets. Rows show the benchmark (DEM-FA30, top) followed by global DEM candidates (SRTM, ASTER, ALOS, FABDEM, GEDTM, DeltaDTM).

Among the corrected products, FABDEM and DeltaDTM produce the most coherent response, suppressing much of the high-frequency noise in SRTM and yielding a continuous

flood surface that preferentially occupies mapped depressions, albeit with a tendency to form compact pools rather than finely channelized inundation. In contrast, GEDTM departs noticeably from this pattern, exhibiting a flood response that is not fully aligned with either FABDEM or DeltaDTM. This behavior suggests a residual vertical and/or smoothing bias similar to ASTER that limits floodplain filling and systematically underestimates flood-prone areas, reducing its suitability in its current form.

The quantitative analysis of flood extents (Figure 14) corroborates the disparity in the hydrological response of the models.

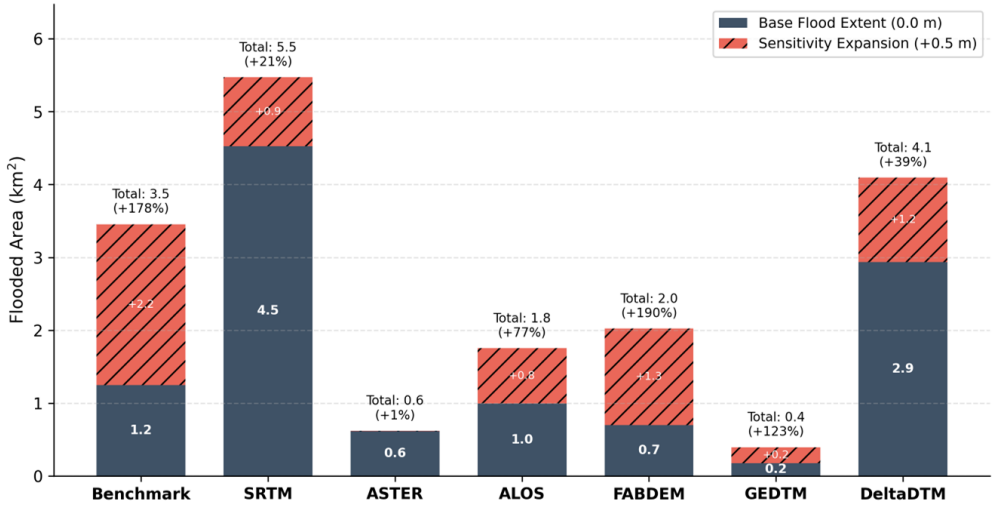

Figure 14. Hydraulic sensitivity (%) for scenarios: base flood extent (0 m) and expansion (0.5 m) in Km^2.

The benchmark establishes critical non-linear dynamics: a 0.5 m water level rise almost triples the flooded area (from 1.2 to 3.5 km², +178%), indicating a very flat plain where small vertical changes drive large lateral expansion. FABDEM is again the only global DEM that closely reproduces this elastic behavior, with a comparable relative growth (+190%, from 0.7 to 2.0 km²), although starting from a lower baseline. ALOS shows an intermediate response (+77%, 1.0–1.8 km²), whereas SRTM exhibits a strongly damped sensitivity (+21%, 4.5–5.5 km²). ASTER is practically invariant (+1%, 0.6–0.6 km²), confirming its structural limitations for deltaic inundation. GEDTM records a high percentage increase (+123%) but on a very small footprint (0.2–0.4 km²), thus still underestimating the flood-prone area. DeltaDTM displays a moderate expansion (+39%, 2.9–4.1 km²), consistent with a more hydraulically responsive (but less elastic) behavior than the benchmark and FABDEM. Finally, the invariance of ASTER suggests severe structural limitations for representing inundation in deltaic regions. These patterns suggest that only DEMs combining effective bare-earth correction (FABDEM and, to a lesser extent, DeltaDTM) could realistically reproduce the non-linear flood sensitivity required for credible hazard assessment in such flat coastal plains.

3.5. Roughness Assessment

Figure 15 illustrates the Roughness Inflation Index (RII), which quantifies the relative surface roughness fidelity of candidate DEMs against the DEM-FA30 benchmark. GEDTM (1.02) shows near-parity with the reference. In contrast, ASTER (4.64), SRTM (3.42), and ALOS (1.86) exhibit marked roughness inflation (RII > 1), consistent with spurious micro-topography that may disrupt floodplain connectivity. FABDEM (0.66) and DeltaDTM (0.71) yield an RII < 1, indicating smoother surfaces relative to the benchmark and potential over-smoothing.

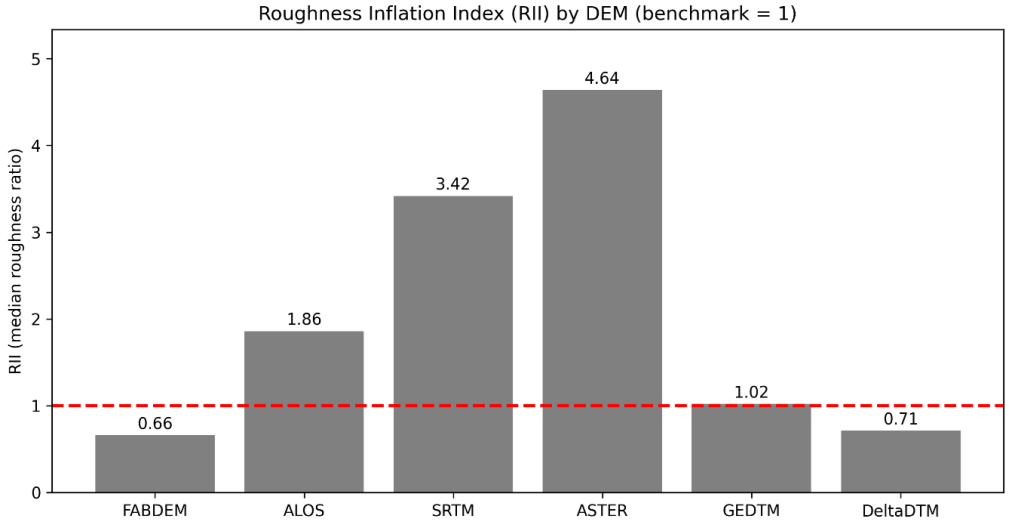

Figure 15. RII (Roughness Inflation Index): Ratio of median local roughness (3 × 3 max–min) for each candidate DEM relative to DEM-FA30 benchmark. RII = 1 indicates parity (red dashed line); RII > 1 reflects inflated micro-topography (spurious artifacts), whereas RII < 1 indicates smoothing relative to reference.

The results identify GEDTM and DeltaDTM as the closest match to the benchmark, whereas the pronounced inflation in ASTER and SRTM suggests that their use in lowland analyses may artificially increase apparent connectivity barriers due to spurious micro-topographic noise.

4. Discussion

4.1. DEM Vertical Accuracy Assessment

The evaluation results indicate that DeltaDTM, GEDTM and FABDEM have the best proven accuracy in the estimated metrics. This result is consistent with expectations because these are improved versions of other global DEMs. FABDEM is an improved version of the Copernicus DEM [29,30]. DeltaDTM is also generated, improving the Copernicus DEM but also incorporating ICESat-2 and GEDI elevation data [39]. Meanwhile, GEDTM was generated with the fusion of ICESat-2 and GEDI data, incorporating almost 30 billion high-quality points [40]. On the other hand, the errors found in the ASTER, SRTM, and ALOS DEMs are within the expected range for this type of model [56]. In addition to being reprocessed DEMs, DeltaDTM, GEDTM, and FABDEM also differ from the others in terms of age. ASTER, SRTM, and ALOS are older missions than Copernicus, ICESAT-2 and GEDI, from which DeltaDTM, GEDTM, and FABDEM are derived [21,57]. This factor also influences the accuracy of DEMs, due to changes in the surface in terms of coverage and interventions, which, in an area of urban growth, can significantly modify the surface.

The error metrics used in this study are widely used in the field of geosciences and for evaluating the vertical accuracy of elevation models [10,21,29]. They have the advantage of using the same unit as the study variable and are relatively easy to interpret. However, they have a limitation in that they do not fit well with data that do not have a normal distribution [21]. In the case of the DEMs evaluated, this limitation was ruled out with probability density diagrams that showed that the errors followed a normal distribution, validating the choice of metrics.

Land cover strongly modulates vertical errors (Figure 10) [58]. Since legacy global DSMs retain canopy and built structure signals, the critical driver is the efficacy of the DeltaDTM and FABDEM artifact removal algorithm. DeltaDTM exhibits an equalized RMSE over land cover categories, while FABDEM has an elevated RMSE in dense vegetation

and sparse vegetation. GEDTM also shows a high RMSE for dense vegetation, which can be evidence of the difficulty that the ICESAT and GEDI sensors have in penetrating vegetation, from where the elevation data was derived [40]. For areas covered by buildings, DeltaDTM, GEDTM and FABDEM perform better than SRTM and ASTER. The same behavior was observed for the bare soil category.

4.2. Hydrological Connectivity DEM Performance

Assessing DEM suitability for hydrological applications requires moving beyond pointwise vertical error metrics to evaluate spatial connectivity and topographic sensitivity. Despite the previously noted X-band limitations in dense canopy land cover, bare-earth global models approximates the benchmark's hydrological response. Drainage network extraction corroborates FABDEM's superiority, achieving the highest consistency with the reference network (F1 score = 0.292 at 30 m), whereas SRTM and ALOS produce fragmented networks with high omission rates due to surface noise. DeltaDTM and GEDTM (representative next-generation global DTMs) show drainage extraction performance close to the local benchmark, supporting their suitability for connectivity-focused hydrologic analyses in low-relief settings. The static flood (bathtub) assessment further revealed how these errors propagate into inundation mapping: the benchmark exhibited a non-linear response, with a +0.5 m water level rise yielding a 191% increase in the flooded area.

FABDEM was the only global product to approximate this sensitivity (185%), suggesting that its filtering effectively restores the lateral connectivity of the bare earth. In contrast, the uncorrected DSMs (SRTM, ALOS) showed attenuated expansion (22% and 80%, respectively), where residual roughness acts as an artificial topographic that partitions the floodplain, while ASTER remained nearly invariant (0%). Surprisingly, despite their strong performance in drainage network extraction, DeltaDTM and GEDTM did not exhibit comparable hydraulic sensitivity. This indicates that capturing drainage topology is not sufficient to reproduce inundation response in low-relief deltas, where small differences in absolute elevation, subtle floodplain thresholds, and local micro-topography can strongly modulate flood extent expansion under a static stage increase. A plausible explanation for this is a residual vertical offset observed relative to the benchmark/GNSS reference (Figures 6 and 7), which can disproportionately affect area–stage sensitivity even when drainage patterns appear.

Recent studies corroborate these findings; Ref. [59] demonstrated that FABDEM consistently outperforms uncorrected DSMs like SRTM in flood-prone environments by removing vegetation biases that obstruct flow paths. Similarly, the hydrology evaluations in [60] confirm that while FABDEM improves general floodplain connectivity, local discrepancies in channel geometry often necessitate hydro-conditioning to fully resolve complex drainage networks.

Nevertheless, considering its favorable hydrological sensitivity response, it is important to note that FABDEM does not spatially replicate the inundation extents of the benchmark with high geometric fidelity. Visually, its flood pattern tends to form compact, pooled areas rather than accurately following the fine, dendritic structure of natural channels.

This spatial discrepancy suggests that the artifact removal algorithm, while effectively correcting the general vertical bias, may inadvertently smooth out critical micro-topography (such as channels, as found in this study) or leave residual roughness that could locally divert flow, as also shown in [61]. Consequently, FABDEM should be regarded as a baseline model with potential for improvement. Its suitability for detailed hydraulic modeling could be significantly enhanced through hydro-conditioning techniques, as proposed in [62].

The integration of pre-existing 2D vector data (e.g., drainage networks) or pre-existing altimetry to "burn in" channel bathymetry would help constrain flow paths like the proposed "fluvial domain method" [63], which could effectively combine FABDEM's superior vertical sensitivity with the horizontal precision needed for local-scale applications.

Future work will focus on exploring these hydro-conditioning strategies, specifically testing the fusion of next-generation models (e.g., DeltaDTM or GEDTM) with vector-based drainage enforcement and bathymetric estimation in order to improve local-scale flood mapping accuracy. Future work should also test these findings against next-generation models (e.g., FathomDEM), whose feature-based corrections could yield distinct hydrologic outcomes.

Beyond vertical statistics, roughness-related descriptors (e.g., local elevation variability, slope/curvature stability) can help explain why small artifacts fragment connectivity in flat terrain; incorporating such diagnostics is a valuable extension for future work [57].

5. Conclusions

The DeltaDTM and GEDTM models showed the best altimetric performance among the DEMs evaluated, with the lowest MAE (0.86 and 0.94) and RMSE (1.17 and 1.26), respectively, followed by FABDEM, with metrics of 1.28 and 1.74, respectively. Altimetric errors are influenced by ground cover. They are greater in areas of dense vegetation and urbanized areas. This variability highlights the importance of analyzing surface characteristics when selecting a DEM for accuracy analysis.

The use of DeltaDTM or similar corrected models is recommended over base models such as SRTM, ASTER, and ALOS. For coastal zones below 30 m, DeltaDTM is better; for areas above 30 m, the use of GEDTM or FABDEM is recommended.

The use of GNSS-RTK ground control points as a reference is a robust tool for validating elevation models, especially in flat areas where small differences can have significant implications in various applications, such as hydrodynamic modeling.

Regarding hydrological connectivity, the analysis confirmed FABDEM's superiority in reproducing drainage structures, achieving the highest geometric agreement with the reference network (F1 = 0.292). DeltaDTM and GEDTM also showed strong drainage representation and comparable network extraction skills, supporting their utility for connectivity-focused applications, although their hydraulic sensitivity remained more dependent on local elevation offsets and floodplain micro-topography. In contrast, SRTM and ALOS generated fragmented networks with high omission rates, proving inadequate for defining flow paths in low-relief terrain. Furthermore, the static flood sensitivity assessment revealed that FABDEM is the only global model capable of replicating the dynamic response of the benchmark, exhibiting an analogous flood area expansion rate (185% vs 191%) under water level increases. Conversely, the uncorrected DSMs (STRM/ASTER/ALOS) displayed attenuated expansion due to artifact-induced roughness, which acts as a barrier to lateral flow propagation.

Local adjustments and specific validations should be considered based on coverage and available data. Future work will focus on improving the local performance of FABDEM, DeltaDTM, and GEDTM through targeted hydro-conditioning and vertical alignment.

Author Contributions: J.M.F.A. and J.R.E.V.: methodology conceptualization; J.M.F.A., J.R.E.V. and J.I.P.-M.: writing; J.M.F.A. and J.R.E.V.: GIS elaboration; J.M.F.A., J.R.E.V. and J.I.P.-M.: review and editing; J.I.P.-M.: supervision; J.R.E.V.: funding management. All authors have read and agreed to the published version of the manuscript.

Funding: This research and the associated article processing charge (APC) were funded by Colombia's Ministerio de Ciencia, Tecnología e Innovación (Minciencias) under Call No. 890-2020 (Project No.

82207), with funds administered by the Instituto Colombiano de Crédito Educativo y Estudios Técnicos en el Exterior (ICETEX).

Data Availability Statement: The data presented in this study, which is not of the public domain, is available upon request from the corresponding author.

Acknowledgments: We thank the University de La Guajira for the contributions to J.I.P.-M., J.R.E.V. and J.M.F.A. to allocate time to this project. Special thanks to Fondo Adaptación de Colombia for providing the aerial photography data necessary to generate the benchmark DEM.

Conflicts of Interest: The authors declare no conflicts of interest.

References

1. Wohl, E. An Integrative Conceptualization of Floodplain Storage. *Rev. Geophys.* **2021**, *59*, e2020RG000724. [CrossRef]
2. Carling, P.A.; Hargitai, H. Floodplain. In *Encyclopedia of Planetary Landforms*; Springer: Berlin/Heidelberg, Germany, 2021; pp. 1–5. [CrossRef]
3. Leal Filho, W.; Azul, A.M.; Brandli, L.; Lange Salvia, A.; Wall, T. Floodplain. In *Life Below Water*; Springer International Publishing: Cham, Switzerland, 2022; p. 419. [CrossRef]
4. Hoitink, A.J.; Nittrouer, J.A.; Passalacqua, P.; Shaw, J.B.; Langendoen, E.J.; Huismans, Y.; van Maren, D.S. Resilience of River Deltas in the Anthropocene. *J. Geophys. Res. Earth Surf.* **2020**, *125*, e2019JF005201. [CrossRef]
5. Borzi, G.; Cellone, F.; Tanjal, C.; Melendi, E.; Carol, E.; Borzi, G.; Cellone, F.; Tanjal, C.; Melendi, E.; Carol, E. Methodological proposal for the study of floods in plains areas with a lack of information. *DYNA* **2020**, *87*, 221–228. [CrossRef]
6. Chen, X.; Yu, M.; Liu, C.; Wang, R.; Zha, W.; Tian, H. Topological and dynamic complexity of the Pearl River Delta and its responses to human intervention. *J. Hydrol.* **2022**, *608*, 127619. [CrossRef]
7. Mazzoleni, M.; Mård, J.; Rusca, M.; Odongo, V.; Lindersson, S.; Di Baldassarre, G. Floodplains in the Anthropocene: A Global Analysis of the Interplay Between Human Population, Built Environment, and Flood Severity. *Water Resour. Res.* **2021**, *57*, e2020WR027744. [CrossRef]
8. Muthusamy, M.; Casado, M.R.; Butler, D.; Leinster, P. Understanding the effects of Digital Elevation Model resolution in urban fluvial flood modelling. *J. Hydrol.* **2021**, *596*, 126088. [CrossRef]
9. Guth, P.L.; Van Niekerk, A.; Grohmann, C.H.; Muller, J.P.; Hawker, L.; Florinsky, I.V.; Gesch, D.; Reuter, H.I.; Herrera-Cruz, V.; Riazanoff, S.; et al. Digital elevation models: Terminology and definitions. *Remote Sens.* **2021**, *13*, 3581. [CrossRef]
10. Meadows, M.; Wilson, M. A Comparison of Machine Learning Approaches to Improve Free Topography Data for Flood Modelling. *Remote Sens.* **2021**, *13*, 275. [CrossRef]
11. Mohanty, M.P.; Nithya, S.; Nair, A.S.; Indu, J.; Ghosh, S.; Mohan Bhatt, C.; Srinivasa Rao, G.; Karmakar, S. Sensitivity of various topographic data in flood management: Implications on inundation mapping over large data-scarce regions. *J. Hydrol.* **2020**, *590*, 125523. [CrossRef]
12. Escobar Villanueva, J. Contribuciones Metodológicas Para la Obtención de Información Altimétrica Requerida en la Evaluación Local de Amenazas por Inundaciones a Partir de Nuevas Tecnologías Geoespaciales. Ph.D. Thesis, Universidad Politécnica de Madrid (UPM), Madrid, Spain, 2020.
13. Guan, L.; Hu, J.; Pan, H.; Wu, W.; Sun, Q.; Chen, S.; Fan, H. Fusion of public DEMs based on sparse representation and adaptive regularization variation model. *ISPRS J. Photogramm. Remote Sens.* **2020**, *169*, 125–134. [CrossRef]
14. Musa, Z.N.; Popescu, I.; Mynett, A. A review of applications of satellite SAR, optical, altimetry and DEM data for surface water modelling, mapping and parameter estimation. *Hydrol. Earth Syst. Sci. Discuss* **2015**, *12*, 4857–4878. [CrossRef]
15. Yamazaki, D.; Ikeshima, D.; Tawatari, R.; Yamaguchi, T.; O'Loughlin, F.; Neal, J.C.; Sampson, C.C.; Kanae, S.; Bates, P.D. A high-accuracy map of global terrain elevations. *Geophys. Res. Lett.* **2017**, *44*, 5844–5853. [CrossRef]
16. W.V.N., S.; W.A.K.I., W.; D.T.N., J.; W.V.D., P. Single Comprehensive Digital Elevation Model for Sri Lanka: Modified Advanced Land Observing Satellite (ALOS) Radiometrically Terrain Corrected (RTC) Products. In *45th Asian Conference on Remote Sensing, ACRS 2024*; Asian Association on Remote Sensing: Colombo, Sri Lanka, 2024.
17. Azizian, A.; Brocca, L. Determining the best remotely sensed DEM for flood inundation mapping in data sparse regions. *Int. J. Remote Sens.* **2020**, *41*, 1884–1906. [CrossRef]
18. Peña, F.; Nardi, F.; Melesse, A.; Obeysekera, J. Assessing geomorphic floodplain models for large scale coarse resolution 2D flood modelling in data scarce regions. *Geomorphology* **2021**, *389*, 107841. [CrossRef]
19. Peramuna, P.D.; Neluwala, N.G.; Wijesundara, K.K.; DeSilva, S.; Venkatesan, S.; Dissanayake, P.B. Enhancing 2D hydrodynamic flood model predictions in data-scarce regions through integration of multiple terrain datasets. *J. Hydrol.* **2025**, *648*, 132343. [CrossRef]

20. Bouwer, M.; Garrote, J. Free Global DEMs and Flood Modelling—A Comparison Analysis for the January 2015 Flooding Event in Mocuba City (Mozambique). *Water* **2022**, *14*, 176. [CrossRef]
21. Meadows, M.; Jones, S.; Reinke, K. Vertical accuracy assessment of freely available global DEMs (FABDEM, Copernicus DEM, NASADEM, AW3D30 and SRTM) in flood-prone environments. *Int. J. Digit. Earth* **2024**, *17*, 2308734. [CrossRef]
22. Earth Resources Observation And Science (EROS) Center. *Shuttle Radar Topography Mission (SRTM) 1 Arc-Second Global*; U.S. Geological Survey: Reston, VA, USA, 2017. [CrossRef]
23. Farr, T.G.; Rosen, P.A.; Caro, E.; Crippen, R.; Duren, R.; Hensley, S.; Kobrick, M.; Paller, M.; Rodriguez, E.; Roth, L.; et al. The Shuttle Radar Topography Mission. *Rev. Geophys.* **2007**, *45*, 2004. [CrossRef]
24. Abrams, M. ASTER Global DEM Version 3, and new ASTER Water Body Dataset. In Proceedings of the The International Archives of the Photogrammetry, Remote Sensing and Spatial Information Sciences, Prague, Czech Republic, 12–19 July 2016; pp. 12–19. [CrossRef]
25. Tachikawa, T.; Kaku, M.; Iwasaki, A.; Gesch, D.; Oimoen, M.; Zhang, Z.; Danielson, J.; Krieger, T.; Curtis, B.; Haase, J.; et al. *ASTER Global Digital Elevation Model Version 2—Summary of Validation Results*; U.S. Geological Survey: Reston, VA, USA, 2011.
26. Tadono, T.; Nagai, H.; Ishida, H.; Oda, F.; Naito, S.; Minakawa, K.; Iwamoto, H. Generation of the 30 m-mesh global digital surface model by ALOS-PRIM PRISM. *Int. Arch. Photogramm. Remote Sens. Spat. Inf. Sci.* **2016**, *XLI-B4*, 157–162. [CrossRef]
27. Rizzoli, P.; Martone, M.; Gonzalez, C.; Wecklich, C.; Borla Tridon, D.; Bräutigam, B.; Bachmann, M.; Schulze, D.; Fritz, T.; Huber, M.; et al. Generation and performance assessment of the global TanDEM-X digital elevation model. *ISPRS J. Photogramm. Remote Sens.* **2017**, *132*, 119–139. [CrossRef]
28. Fahrland, E.; Paschko, H.; Jacob, P.; Kahabka, H. *Copernicus DEM Copernicus Digital Elevation Model Product Handbook*; Technical Report; Airbus Defence and Space GmbH: Taufkirchen, Germany, 2022.
29. Hawker, L.; Uhe, P.; Paulo, L.; Sosa, J.; Savage, J.; Sampson, C.; Neal, J. A 30 m global map of elevation with forests and buildings removed. *Environ. Res. Lett.* **2022**, *17*, 24016. [CrossRef]
30. Marsh, C.B.; Harder, P.; Pomeroy, J.W. Validation of FABDEM, a global bare-earth elevation model, against UAV-lidar derived elevation in a complex forested mountain catchment. *Environ. Res. Commun.* **2023**, *5*, 031009. [CrossRef]
31. Chai, L.T.; Wong, C.J.; James, D.; Loh, H.Y.; Liew, J.J.; Wong, W.V.; Phua, M.H. Vertical accuracy comparison of multi-source Digital Elevation Model (DEM) with Airborne Light Detection and Ranging (LiDAR). *IOP Conf. Ser. Earth Environ. Sci.* **2022**, *1053*, 012025. [CrossRef]
32. Marešová, J.; Bašta, P.; Gdulová, K.; Barták, V.; Kozhoridze, G.; Šmída, J.; Markonis, Y.; Rocchini, D.; Prošek, J.; Pracná, P.; et al. Choosing the Optimal Global Digital Elevation Model for Stream Network Delineation: Beyond Vertical Accuracy. *Earth Space Sci.* **2024**, *11*, e2024EA003743. [CrossRef]
33. Nandam, V.; Patel, P.L. A framework to assess suitability of global digital elevation models for hydrodynamic modelling in data scarce regions. *J. Hydrol.* **2024**, *630*, 130654. [CrossRef]
34. Pérez, J.I.; Escobar, J.R.; Fragozo, J.M. Modelación Hidráulica 2D de Inundaciones en Regiones con Escasez de Datos. El Caso del Delta del Río Ranchería, Riohacha-Colombia. *Inf. Tecnológica* **2018**, *29*, 143–156. [CrossRef]
35. Escobar Villanueva, J. *INFORME FINAL MEMORIA DE CÁLCULO Y PRODUCTOS FINALES CONTRATO DE PRESTACION DE SERVICIOS PROFESIONALES NO. 485 DEL 2024*; Technical Report; Universidad de La Guajira: Riohacha, Colombia, 2024.
36. Takaku, J.; Tadono, T.; Tsutsui, K.; Ichikawa, M. VALIDATION of "aW3D" GLOBAL DSM GENERATED from ALOS PRISM. *ISPRS Ann. Photogramm. Remote Sens. Spat. Inf. Sci.* **2016**, *3*, 25–31. [CrossRef]
37. Japan Aerospace Exploration Agency. *ALOS World 3D 30 Meter DEM. V3.2, Jan 2021*; Technical Report; Japan Aerospace Exploration Agency—Distributed by OpenTopography: Tokyo, Japan, 2021.
38. NASA; METI; AIST; Japan Spacesystems and U.S./Japan ASTER Science Team. *Global Digital Elevation Model V003 [Data Set]*; Technical Report; NASA: Washington, DC, USA, 2019.
39. Pronk, M.; Hooijer, A.; Eilander, D.; Haag, A.; de Jong, T.; Vousdoukas, M.; Vernimmen, R.; Ledoux, H.; Eleveld, M. DeltaDTM: A global coastal digital terrain model. *Sci. Data* **2024**, *11*, 273. [CrossRef]
40. Ho, Y.; Grohmann, C.H.; Lindsay, J.; Reuter, H.I.; Parente, L.; Witjes, M.; Hengl, T. GEDTM30: Global ensemble digital terrain model at 30 m and derived multiscale terrain variables. *PeerJ* **2025**, *13*, e19673. [CrossRef]
41. Zanaga, D.; Van De Kerchove, R.; Daems, D.; De Keersmaecker, W.; Brockmann, C.; Kirches, G.; Wevers, J.; Cartus, O.; Santoro, M.; Fritz, S.; et al. *ESA WorldCover 10 m 2021 v200*; Technicall Report; Zenodo: Genève Switzerland, 2022. [CrossRef]
42. Topcon Corporation. Hiper V Receptor GNSS de Doble Frecuencia. Technicall Report. 2017. Available online: http://eu-dev.topconpositioning.com/sites/default/files/product_files/hiper_v_brochure_c_team_en_eu_low.pdf (accessed on 28 August 2025).
43. Ettritch, G.; Hardy, A.; Bojang, L.; Cross, D.; Bunting, P.; Brewer, P. Enhancing digital elevation models for hydraulic modelling using flood frequency detection. *Remote Sens. Environ.* **2018**, *217*, 506–522. [CrossRef]

44. Han, H.; Zeng, Q.; Jiao, J. Quality Assessment of Three Digital Elevation Models with 30 M Resolution by Taking 12 M TanDEM-X DEM as Reference. In *IGARSS 2020—2020 IEEE International Geoscience and Remote Sensing Symposium*; IEEE: New York, NY, USA, 2020; pp. 5155–5158. [CrossRef]
45. Nandam, V.; Patel, P.L. Assessment of Vertical Accuracy of Freely Available Global Digital Elevation Models for Heterogeneous Terrains in India. *Lect. Notes Civ. Eng.* **2023**, *339 LNCE*, 169–182. [CrossRef]
46. Yap, L.; Ludovic, H.; Kandé, R.; Nouayou, J.; Kamguia, N.; Abdou, N.; Makuate, M.B.; Kandé, H.; Nouayou, R.; Kamguia, J.; et al. Vertical accuracy evaluation of freely available latest high-resolution (30 m) global digital elevation models over Cameroon (Central Africa) with GPS/leveling ground control points. *Int. J. Digit. Earth* **2019**, *12*, 500–524. [CrossRef]
47. Wang, W.; Lu, Y. Analysis of the Mean Absolute Error (MAE) and the Root Mean Square Error (RMSE) in Assessing Rounding Model. *IOP Conf. Ser. Mater. Sci. Eng.* **2018**, *324*, 012049. [CrossRef]
48. Zhao, X.; Yanjun, S.; Tianyu, H.; Chen, L.; Gao, S.; Wang, R.; Jin, S.; Guo, Q. A global corrected SRTM DEM product for vegetated areas. *Remote Sens. Lett.* **2018**, *9*, 393–402. [CrossRef]
49. Kasi, V.; Yeditha, P.K.; Rathinasamy, M.; Pinninti, R.; Landa, S.R.; Sangamreddi, C.; Agarwal, A.; Dandu Radha, P.R. A novel method to improve vertical accuracy of CARTOSAT DEM using machine learning models. *Earth Sci. Inform.* **2020**, *13*, 1139–1150. [CrossRef]
50. Liu, Y.; Bates, P.D.; Neal, J.C.; Yamazaki, D. Bare-Earth DEM Generation in Urban Areas for Flood Inundation Simulation Using Global Digital Elevation Models. *Water Resour. Res.* **2021**, *57*, e2020WR028516. [CrossRef]
51. Ariza-López, F.J.; Reinoso-Gordo, J.F. Comparison of Gridded DEMs by Buffering. *Remote Sens.* **2021**, *13*, 3002. [CrossRef]
52. QGIS Development Team. *QGIS Geographic Information System*; Open Source Geospatial Foundation: Beaverton, OR, USA, 2024.
53. Mcleod, E.; Poulter, B.; Hinkel, J.; Reyes, E.; Salm, R. Sea-level rise impact models and environmental conservation: A review of models and their applications. *Ocean. Coast. Manag.* **2010**, *53*, 507–517. [CrossRef]
54. Sanders, B.F.; Wing, O.E.; Bates, P.D. Flooding is Not Like Filling a Bath. *Earth's Future* **2024**, *12*, e2024EF005164. [CrossRef]
55. GDAL/OGR Contributors. *GDAL/OGR Geospatial Data Abstraction Software Library*; Open Source Geospatial Foundation: Beaverton, OR, USA, 2025. [CrossRef]
56. Courty, L.G.; Soriano-Monzalvo, J.C.; Pedrozo-Acuña, A. Evaluation of open-access global digital elevation models (AW3D30, SRTM, and ASTER) for flood modelling purposes. *J. Flood Risk Manag.* **2019**, *12*, e12550. [CrossRef]
57. Guth, P.L.; Trevisani, S.; Grohmann, C.H.; Lindsay, J.B.; Reuter, H.I. Benchmarking Elevation Plus Land Surface Parameters Finds FathomDEM and Copernicus DEM Win as Best Global DEMs. *Remote Sens.* **2025**, *17*, 3919. [CrossRef]
58. Huang, J.; Yu, Y. Vertical Accuracy Assessment of the ASTER, SRTM, GLO-30, and ATLAS in a Forested Environment. *Forests* **2024**, *15*, 426. [CrossRef]
59. Hawker, L.; Neal, J.; Savage, J.; Kirkpatrick, T.; Lord, R.; Zylberberg, Y.; Groeger, A.; Thuy, T.D.; Fox, S.; Agyemang, F.; et al. Assessing LISFLOOD-FP with the next-generation digital elevation model FABDEM using household survey and remote sensing data in the Central Highlands of Vietnam. *Nat. Hazards Earth Syst. Sci.* **2024**, *24*, 539–566. [CrossRef]
60. Miskin, T.J.; Rosas, L.R.; Hales, R.C.; Nelson, E.J.; Follum, M.L.; Gutenson, J.L.; Williams, G.P.; Jones, N.L. Impact of Elevation and Hydrography Data on Modeled Flood Map Accuracy Using ARC and Curve2Flood. *Hydrology* **2025**, *12*, 202. [CrossRef]
61. Bates, P. Fundamental limits to flood inundation modelling. *Nat. Water* **2023**, *1*, 566–567. [CrossRef]
62. Uhe, P.; Lucas, C.; Hawker, L.; Brine, M.; Wilkinson, H.; Cooper, A.; Saoulis, A.A.; Savage, J.; Sampson, C. FathomDEM: An improved global terrain map using a hybrid vision transformer model. *Environ. Res. Lett.* **2025**, *20*, 034002. [CrossRef]
63. Escobar Villanueva, J.R.; Pérez-Montiel, J.I.; Nardini Cristoforo, A.G. DEM Generation Incorporating River Channels in Data-Scarce Contexts: The "Fluvial Domain Method". *Hydrology* **2025**, *12*, 33. [CrossRef]